Landslides (2012) 9:557–563
DOI 10.1007/s10346-012-0322-z
Received: 23 September 2011
Accepted: 13 February 2012
Published online: 3 March 2012

Honn Kao · Chih-Wen Kan · Rong-Yuh Chen · Chien-Hsin Chang · Andreas Rosenberger · Tzay-Chyn Shin · Pei-Ling Leu · Kai-Wen Kuo · Wen-Tzong Liang

Locating, monitoring, and characterizing typhoon-induced landslides with real-time seismic signals

Abstract Landslides induced by typhoon Morakot during its passage across Taiwan on 7–9 Aug 2009 claimed more than 700 lives and caused heavy economic loss. Unlike earthquake monitoring, precise locations of landslides could not be determined in near-real time because their seismic phases are difficult to identify. Here, we show that large, damaging landslide events are characterized seismically by a distinct waveform pattern of frequent intermixes of *P* and *S* waves over a time window of several tens of seconds. The predominant frequency band during these time windows ranges from 0.5 to 5Hz. The high-frequency content is clearly deficient relative to that of local earthquakes by about one to two orders. We also demonstrate that large landslide events can be located and monitored with algorithms specifically designed for real-time seismic applications. This near-real-time monitoring capability would be particularly useful for emergency responders and government organizations to coordinate effective relief-and-rescue operations.

Keywords Landslides and mud/debris flows · Near-real time · Source-scanning algorithm · Typhoon

Introduction

Landslides induced by the excessive rainfall of typhoons and/or hurricanes can be catastrophic, both in loss of human life and to the economy. Typhoon Morakot, for example, passed over Taiwan on 7–9 Aug 2009 and dumped as much as 1,800 mm of rain over most of the mid- and southern parts of the island (Fig. 1). There were at least 619 fatalities and 76 people missing; most resulted from landslides and mud/debris flows (LMDF) burying villages in the mountainous area. The agricultural loss alone is estimated to be half a billion US dollars. In addition, there was wide-spread damage to transportation networks, levees, critical infrastructures, and other facilities.

Timing is the most critical factor in rescuing LMDF victims. Ideally, emergency response agencies would identify and pin-point the locations of large-scale LMDF as they occur, then dispatch rescue teams as soon as the air and ground conditions permit. In reality, however, the exact location and size of LMDF often cannot be accurately assessed until much later, when surveillance photographs from aircrafts and/or satellites become available. Avoiding such a time delay might significantly improve the efficiency of rescue operations and save hundreds of lives.

Seismic studies of LMDF in the past focused primarily on the representation of equivalent sources (e.g., Brodsky et al. 2003; Dahlen 1993; Kanamori and Given 1982; Kanamori et al. 1984) and the estimation of geometrical parameters such as the mass volume, total drop height, runoff speed, and runoff distance (e.g., Berrocal et al. 1978; Deparis et al. 2008; La Rocca et al. 2004). Although the potential importance of utilizing seismic networks to detect movements of large amount of earth mass has been recognized before (La Rocca et al. 2004; Norris 1994), near-real-time seismic detecting and monitoring of LMDF have yet to be implemented. The difficulty arises mainly from two issues: (1) the seismic signature of LMDF is very complex and cannot be effectively identified without a detailed waveform analysis and (2) the epicenters of LMDF cannot be confidently determined by conventional earthquake-locating methods, mainly due to the lack of clear arrivals of *P* and *S* phases. In this study, we present a solution to the above issues and use the LMDF events induced by typhoon Morakot in Taiwan for demonstration.

Characterize typhoon-induced LMDF waveforms

The physical process of a LMDF event is basically a rapid transportation of earth mass due to gravitational instability that involves falling, breaking, sliding, bouncing/rebounding, and deposition (Deparis et al. 2008; Hungr et al. 2001). The source of a LMDF can be mathematically represented by a single force (Brodsky et al. 2003; Eissler and Kanamori 1987; Kanamori and Given 1982; Kanamori et al. 1984) or a shallow horizontal fault (Dahlen 1993), but such approaches work only for long-period waves. During typhoon Morakot's passage across Taiwan, many seismic events were detected by the regional broadband seismograph network (Broadband Array in Taiwan for Seismology (BATS)) with waveform patterns significantly different from ordinary local earthquakes (Fig. 2). In this section, we investigate these waveforms and show their characteristics.

Characteristics in time domain

In Table 1, we list the BATS stations that have recorded good LMDF signals and the corresponding parameters of individual LMDF events. Two representative waveform examples are shown in Fig. 2 to demonstrate the overall seismic characteristics of LMDF signals. The first noticeable feature is the lack of distinctive arrivals of seismic phases such as *P* or *S*. Instead, the waveforms exhibit a tremor-like pattern with intermittent bursts of large amplitudes.

We subject the recorded waveforms to a real-time ground motion analyzer (Rosenberger 2010). The ground motion analyzer consists of a recursive singular-value-decomposition matrix that maps the three-component seismic data stream from the geographic coordinate system to the principal coordinate system of the particle motions at the resolution of the data sampling interval. If we take the dip angle (θ) of the first eigenvector of the particle motions as a proxy for the overall ground motion, then the functions of $\sin(\theta)$ and $\cos(\theta)$ become effective identifiers (in the range of 0–1) for motions in the vertical and horizontal directions, respectively. Thus, by modulating each seismogram with $\sin(\theta)$ and with $\cos(\theta)$, we can effectively split a waveform (black traces, Fig. 2) into two traces that show significant signals when the ground is dominated by motions closer to the vertical axis

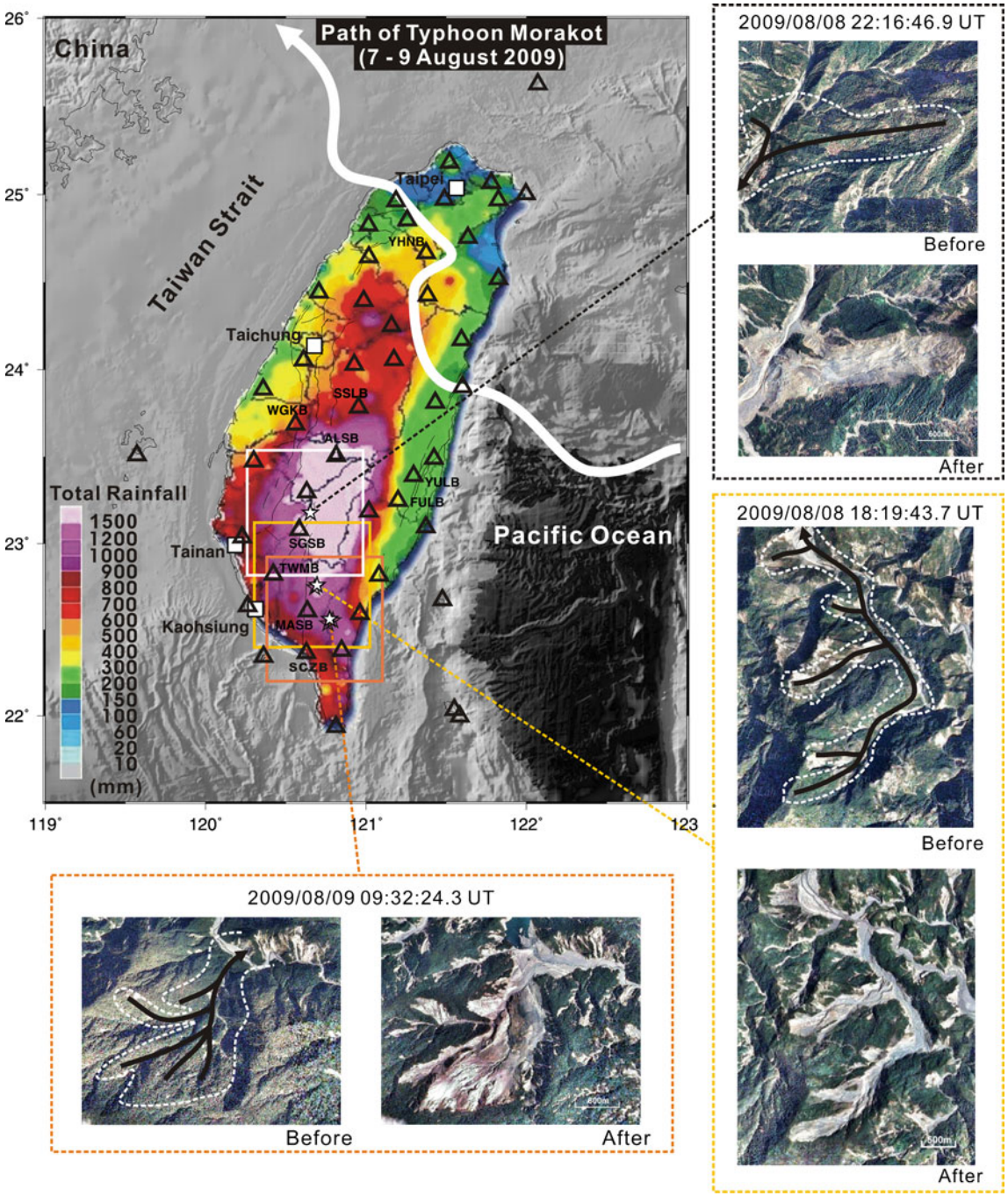

Fig. 1 Map showing the path of typhoon Morakot across Taiwan in Aug 2009. *Stars* mark epicenters of typhoon-induced large-scale LMDF as determined by this study. Satellite images before and after Morakot for three representative cases (*white stars*) are shown with *dashed white lines* marking the approximate perimeters of the corresponding LMDF. *Thick lines with arrows* indicate the general directions of mass flow. *Large rectangles* on the map correspond to the boundaries of source images shown in Fig. 5. *Open triangles* mark the station locations of the BATS. Major cities in Taiwan are marked by *white squares*

(presumably corresponding to primary waves, blue traces, Fig. 2) and to the horizontal plane (presumably shear waves, red traces, Fig. 2), respectively.

Our results suggest that the most characteristic feature of LMDF waveforms is the frequent switch between high and low dip angles of the particle motions (light blue and pink strips, respectively; Fig. 2). This is in sharp contrast to the pattern of an ordinary local earthquake whose *P* and *S* wave trains can be easily recognized (Fig. 2c). In some cases, the LMDF waveforms appear to have equal amounts of *P* and *S* energies (yellow stripes, Fig. 2), but most such occasions are observed in the middle portion of LMDF signals where the amplitudes are relatively large.

The intermittent bursts of *P* and *S* phases are obviously related to the dynamic history of individual LMDF events. As an LMDF event is initiated, the downward-sliding mass interacts

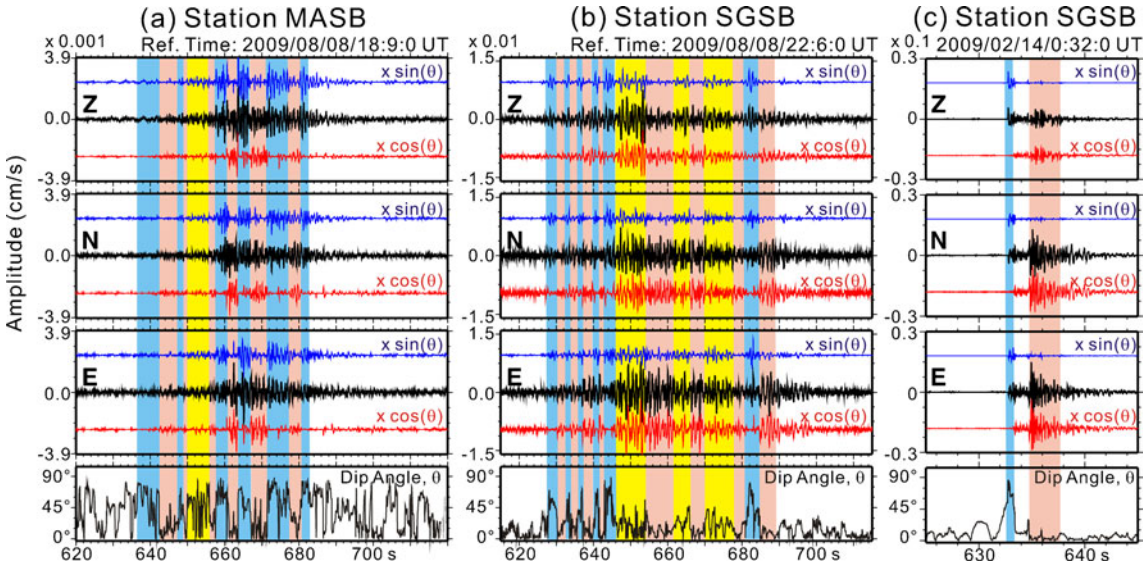

Fig. 2 Real-time ground motion analysis of the three-component, broadband seismograms (*black traces*) recorded by two stations of the BATS. **a**, **b** Two LMDF events that were induced by typhoon Morakot; **c** a local earthquake. The dip angle of the principal ground motion as a function of time (θ) is shown at the bottom. *Light blue and pink stripes* mark time windows when the ground motions are associated with large and small dip angles (presumably corresponding to *P* and *S* waves), respectively. *Yellow stripes* indicate possible overlapping arrivals of both phases. Each waveform can be split into two traces (*blue and red traces*) by modulating with sin(θ) and cos(θ), respectively, to emphasize the corresponding *P* and *S* energies. LMDF signals are characterized by frequent intermix of *P* and *S* waves over a time window of several tens of seconds while ordinary earthquake signals have well separated *P* and *S* phases

with the underlying ground and transfers part of its kinematic energy into seismic energy. Thus, the number, amplitude and timing of the intermittent energy bursts for individual LMDF events may be very different depending on the exact ground conditions (e.g., Fig. 2a, b). After carefully examining all the LMDF waveforms recorded by BATS, we found that the frequent intermix of *P* and *S* phases over a time window of several tens of seconds appears to be a robust feature to characterize LMDF signals.

Characteristics in frequency domain

Another distinct seismic signature of LMDF is their frequency characteristics. To exploit the spectral detail at the highest resolution, we calculate the instantaneous frequencies and their spectral amplitudes for each time instance using the Hilbert–Huang Transform (HHT) (Huang et al. 1996; Huang and Wu 2008). Unlike moving window Fast Fourier Transform (FFT) or wavelet transform that may suffer from limited time-frequency resolution due to their a priori mathematical basis, the HHT is designed to specifically analyze nonlinear and non-stationary signals. The HHT consists of two major components, namely the empirical mode decomposition and Hilbert spectral analysis, that adapt to the spectral nature of the input data. For more details on HHT's theory and technical applications, readers are referred to the web page of the Research Center for Adaptive Data Analysis of the National Central University, Taiwan, at http://rcada.ncu.edu.tw/intro.html.

We apply the HHT to the vertical component of broadband seismograms in Fig. 2, and the corresponding HHT spectrograms are shown in Fig. 3. Our results indicate that the predominant frequency band of the LMDF signals is between 0.5 and 5 Hz (Fig. 3a, b). Some particularly stronger bursts (mostly corresponding to *P* waves) have slightly richer spectral contents, but all appear to be below ~10 Hz. In comparison, the *P* and *S* phases of a local earthquake exhibit a much wider spectral content

Table 1 List of landslide events induced by typhoon Morakot and their source parameters

Event time (UT)	Latitude (°N)	Longitude (°E)	Area (km^2)	Seismograph stations with visible signals	Minimum distance to station (km)	Magnitude (M_L)
8 Aug 2009 17:06:09.9	22.557	120.792	0.68	MASB, SCZB, and YULB	36.8	2.3
8 Aug 2009 18:19:43.7	22.761	120.696	1.35	MASB, TWMB, SCZB, and YULB	19.8	2.6
8 Aug 2009 20:16:32.2	22.54	120.764	0.72	MASB, SCZB, and TWMB	15.6	2.5
9 Aug 2009 22:16:46.9	23.176	120.652	2.40	SGSB, FULB, YULB, and YHNB	10.3	2.7
9 Aug 2009 9:32:24.3	22.563	120.774	2.40	MASB, SCZB, FULB, and YULB	15.6	2.9

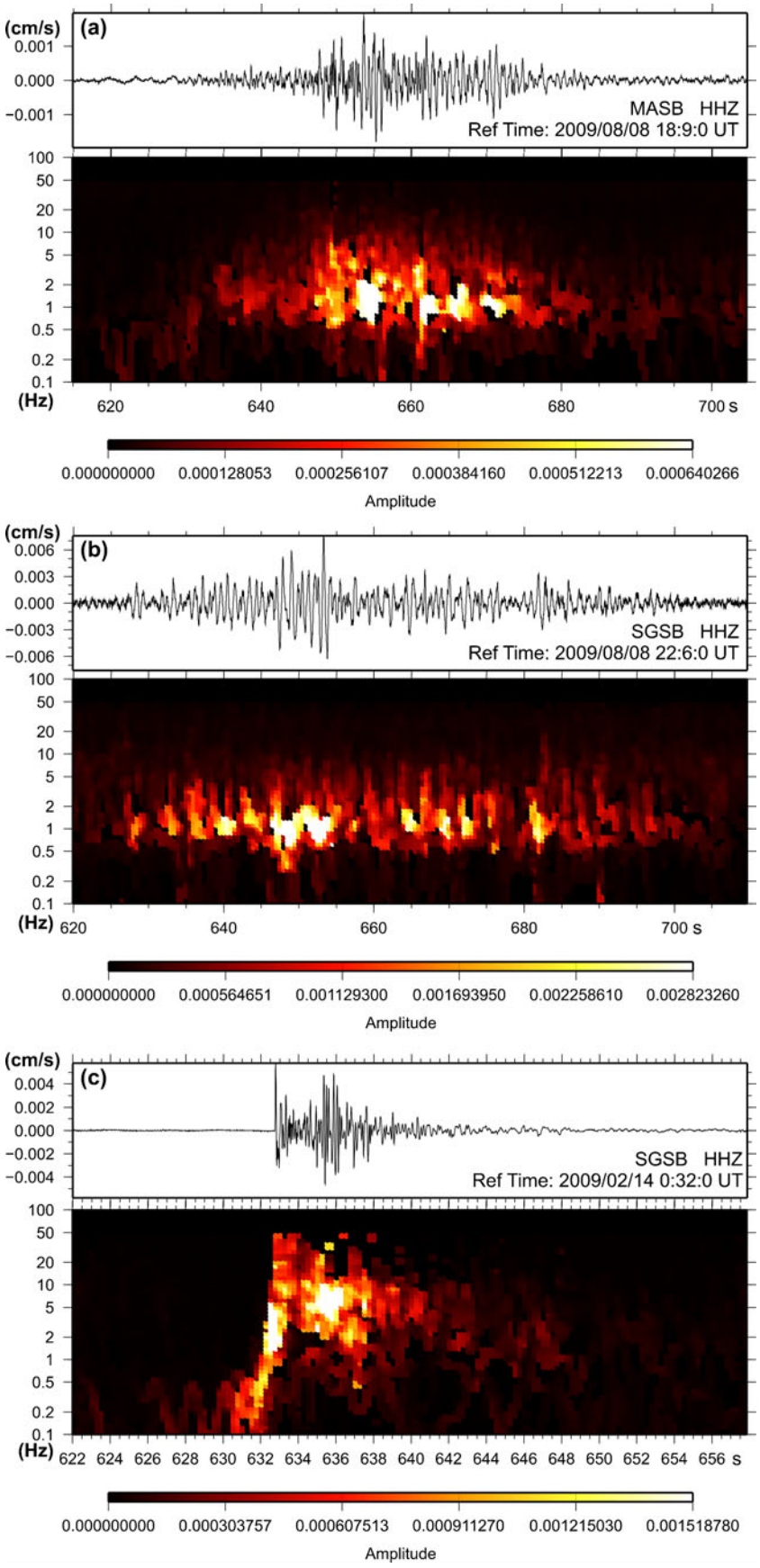

Fig. 3 HHT of broadband seismograms of two LMDF events (**a**, **b**) and one local earthquake (**c**). Vertical components of the original waveforms in Fig. 2 are shown on the *top*, whereas the corresponding HHT spectrograms are shown at the bottom. The LMDF signals have a predominant band of instantaneous frequencies between 0.5 and 5 Hz with intermittent bursts of seismic energy. In contrast, the *P* and *S* phases of a local earthquake exhibit a much wider spectral content with frequencies up to ~50 Hz

with frequencies up to ~50 Hz (Fig. 3c). The pattern of intermittent bursts of seismic energy is clearly visible on the HHT spectrograms of LMDF signals but not for most of local earthquakes.

In Fig. 4, we show the conventional FFT spectra of the seismic signals of LMDF and compare them to local earthquakes. Each group is normalized against its respective average background noise to have approximately the same amplitude at 0.1–0.3 Hz. All spectra are derived from the vertical component of the broadband seismograms from stations listed in Table 1.

It becomes apparent that the spectra of LMDF events are on average one to two orders smaller than those of local earthquakes for frequencies >1 Hz. However, the fall-off rate at high frequencies is not as dramatic as that for explosive sources (e.g., quarry blasts; Allmann and Shearer 2008), suggesting that a significant amount of shear deformation must have been involved in the LMDF source process. We conclude that the deficiency of high-frequency content and the inter-mixed pattern of *P* and *S* waves can be used as important first-order discriminators for LMDF events from other seismic sources.

Locating LMDF in near-real time

The source locations of the tremor-like LMDF signals are difficult to determine using conventional earthquake-locating routines that rely on precise arrival times of seismic phases (e.g., Tsai and Wu 1997). We adopt the innovative Source-Scanning Algorithm (SSA) that was originally designed to locate non-volcanic tremor along subduction zones (Kao and Shan 2004; Kao et al. 2005). In this section, we first briefly describe the theory of SSA and the modifications that we have made in data processing to suit the LMDF conditions, and then provide three representative examples.

Theory

The SSA systematically searches the model space for possible existence of seismic sources according to the "brightness" function of each origin time and hypocenter combination (Kao and Shan 2004). Given a combination of time (τ) and location (η), the corresponding brightness function is defined as

$$br(\eta,\tau)=\frac{1}{N}\sum_{n=1}^{N}\left\{\frac{\sum_{m=-M_1}^{M_2}\left[W_m\cdot U_n\left(\tau+t_{\eta n}+m\delta t\right)\right]}{\sum_{m=-M_1}^{M_2}W_m}\right\} \quad (1)$$

where U_n is the normalized waveform envelope recorded at station n; $t_{\eta n}$ is the calculated travel time from point η to station n; N is the total number of stations; M_1 and M_2 are the numbers of samples before and after the predicted arrival time (i.e., $\tau+t_{\eta n}$), respectively; m is the index of a sample point within the window defined by M_1 and M_2; δt is the sampling interval; and W_m is the weighting factor.

When a significant seismic source exists at the given location and time, the corresponding brightness function increases (i.e., becomes a bright spot) because the observed amplitudes at the predicted arrival times (i.e., $\tau+t_{\eta n}$) are systematically large for all stations. Similarly, the brightness is dimmed if the given location-time combination is inconsistent with the arrivals of large amplitudes at most stations. Thus, by systematically scanning the entire area at incremental time steps, the spatiotemporal distribution of LMDF sources can be illuminated by the brightness functions, and the brightest spots are deemed the most likely source locations (Kao and Shan 2007).

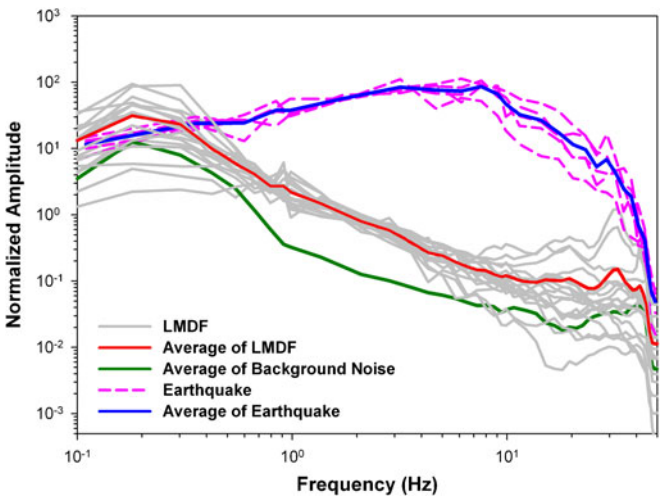

Fig. 4 FFT spectra of LMDF events induced by typhoon Morakot and of local earthquakes. All seismograms are taken from the vertical component of stations listed in Table 1. Each group is normalized against its respective average background noise to have approximately the same amplitude at 0.1–0.3 Hz. Seismic signals of LMDF are one to two orders deficient in the high frequency content (1–30 Hz) with respect to that of local earthquakes

Data processing and analysis

The BATS (Fig. 1) was established in the mid-1990s to provide real-time, continuous broadband seismic data for the Taiwan region (Kao et al. 1998). BATS is now jointly operated by the Institute of Earth Sciences, Academia Sinica, and the Seismological Observation Center of the Central Weather Bureau (CWB) of Taiwan. After BATS signals are transmitted back to the CWB data center, they are unified to the same instrument response and then band-passed between 1 and 8 Hz to remove long-period background noise. The maximum horizontal amplitude (as constructed from the two horizontal components) at each time step is used to construct the waveform envelope for each station (i.e., U_n in Eq. 1). If the horizontal components are not usable (due to signal interruption, clipping, excessive noise, etc.), the vertical component is used instead.

A specific modification we made to the original SSA analysis is the automatic ground motion filtering at the end of data processing to split each seismogram into two traces according to the principal particle motion's dip angle at each time instance (Fig. 2). Because all arrival times in the calculation of brightness functions are based on the regional *S* velocity model, it becomes critical to use only the red traces in the scanning process to minimize any brightness contribution from *P*. Experiments with and without ground motion filtering indicate that ground motion filtering reduces the uncertainty of final epicentral locations by as much as 30%.

The scanning process is performed in three stages. The first stage scans the entire model at a spatial interval of 10 km and with a time increment of 5 s. This stage can quickly identify the possible existence of seismic sources and their approximate locations and time windows. For most cases, this stage can be finished within 1 min of the seismograms being collected, and the source information can be passed immediately to emergency response agencies for their reference. In the second and third stages of scanning, successively

finer grids and time steps are adopted to obtain the optimal time-location combination (4-km interval at 1-s time step in the second stage and 1 km at 0.1 s in the third). Because the fine scanning is limited to the vicinity of the best solution(s) obtained in the previous stage, the required processing time can be greatly reduced to satisfy the criterion of near-real-time monitoring.

Representative examples

The SSA analysis of the tremor-like waveforms recorded during the passage of typhoon Morakot pinpoints the source locations to within a few km from the places where large-scale LMDF are later identified on satellite images (Figs. 1 and 5). The determined origin times of these events are also consistent with the accounts of LMDF survivors, as reported by the local news media. For all LMDF we have studied, final solutions were obtained within 2 min from the start of SSA calculation. Based on the determined source parameters and the observed maximum amplitudes measured from individual seismograms, the equivalent seismic magnitudes of the LMDF events were estimated to range from M_L of ~2.2 to 2.9.

Three representative examples of locating LMDF using SSA are shown in Fig. 5. For each event, a snapshot of the normalized brightness function at the estimated origin time is plotted in the lower panel to illuminate the source distribution. The brightest spot, marked by a star, is deemed to be the most likely location (i.e., the centroid) of each LMDF event because it best matches the arrivals of large bursts of seismic energy at multiple stations (upper panel, Fig. 5). It is important to realize that the observed multiple bursts in LMDF waveforms may be associated with sources scattered over a finite time and space. While theoretically it is possible to delineate a complete spatiotemporal distribution of all sources (Kao and Shan 2007), in reality smaller sources can be difficult to identify, and their solutions often have large uncertainties due to imperfect station coverage and poor waveform quality (i.e., insufficient signal-to-noise ratios). Our results indicate that the brightest spot of an SSA image can reasonably represent the bulk location of a LMDF event where subsequent rescue operations, if needed, should be given top priority.

Discussion and conclusion

Since SSA is a mapping process that translates the observed seismic amplitudes from the time-space domain at stations to the time-space domain at the source (Kao and Shan 2004), each seismic burst can correspond to an infinite number of sources as long as the observed arrival time is consistent with the assumed combinations of origin time and epicenter. Only the assumed origin time and epicenter that correspond to the true source can, however, correctly predict the arrival of large amplitudes at multiple stations. In other words, the accuracy of SSA solutions can be rapidly improved in a near-real-time system as additional waveforms from nearby stations are incrementally added to the analysis.

While the brightest spots on the SSA images (Fig. 5) are interpreted as the centroid locations of the corresponding LMDF, isolated

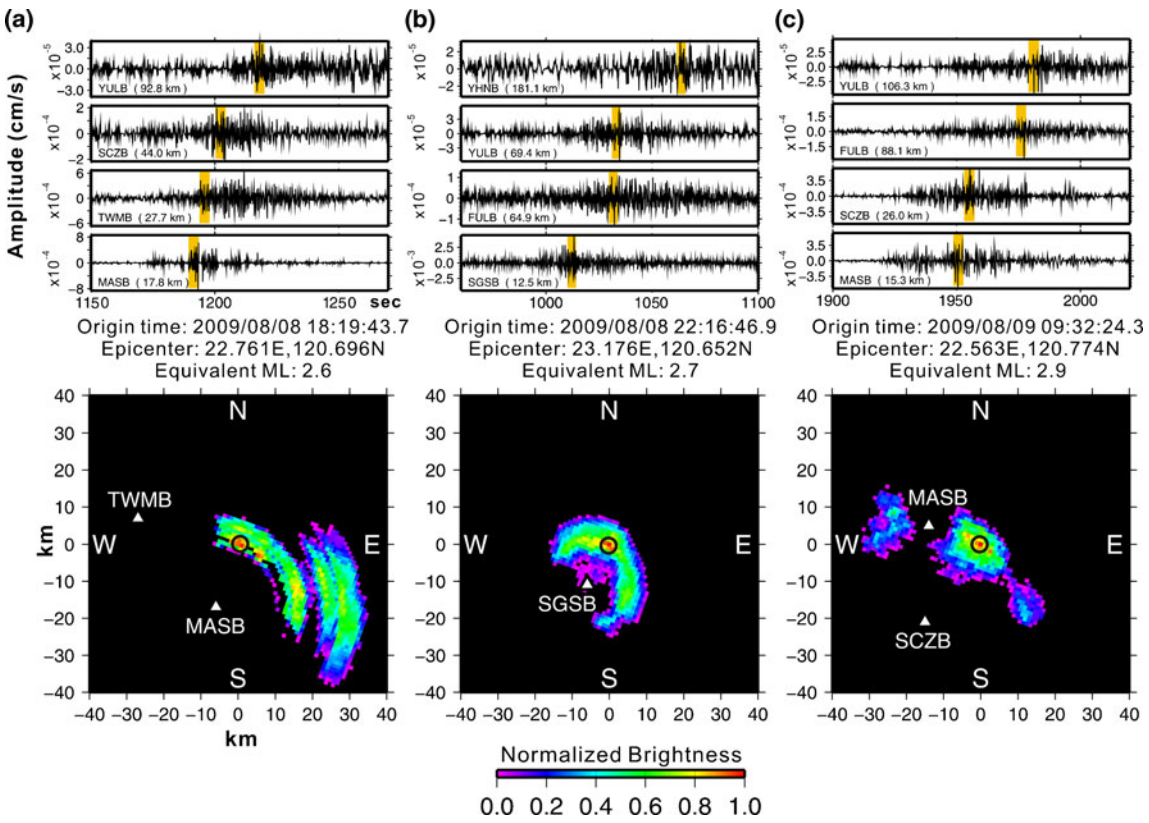

Fig. 5 Representative examples of LMDF epicenters located from real-time seismic observations using SSA: **a** one of the earliest induced LMDF, **b** that responsible for the most casualties, and **c** that with the largest equivalent seismic magnitude. Source scanning is done in three stages with increasing time and space resolution to maximize calculation efficiency. *Orange bars* mark the predicted arrival times at selected stations from the determined origin times and epicenters. Snapshots of the normalized brightness functions at the corresponding origin times are shown in the *lower panel*. The most likely locations of LMDF sources are illuminated as the brightest spots (*encircled*). *Triangles* mark the locations of nearby broadband seismic stations

brightness peaks are found within 10 km in the surrounding area. One possible explanation is that they correspond to other induced LMDF events in the same area, but smaller in size. Given the widespread LMDF later identified from satellite images (Fig. 1), this scenario appears to be highly possible. Since a detailed inversion of the kinematic process of LMDF is beyond the scope of this study, we shall address the issue of delineating secondary LMDF sources in a separated paper.

Although near-real-time monitoring of significant earthquakes has been established for many years, the progress in near-real-time monitoring, characterizing, and locating LMDF is very limited thus far. Our analysis of the broadband seismic records of typhoon-induced LMDF indicates they have two distinct seismic signatures: tremor-like waveforms with frequent intermixes of *P* and *S* waves and a predominant frequency band of 0.5–5 Hz over a time window of several tens of seconds. By utilizing algorithms specifically designed for real-time applications, we demonstrate that LMDF can be recognized, monitored and located much more effectively than before. The success of near-real-time analysis of LMDF signals not only offers a new way to conduct LMDF research in the future, but also has a significant societal impact as the near-real-time LMDF monitoring system is incorporated into government emergency response plans. The benefit of possibly saving numerous LMDF victims via rapid rescue efforts is invaluable.

Acknowledgments

We thank Cheng-Chien Liu for providing the satellite images shown in Fig.1, Yi-Ben Tsai for stimulating discussion and suggestions, an anomalous reviewer (external), and Alison Bird (internal) for reviewing the manuscript. SAC and GMT are used to process data and to generate figures. ESS/GSC contribution no. 20110361.

References

Allmann BP, Shearer PM (2008) Spectral discrimination between quarry blasts and earthquakes in southern California. Bull Seismol Soc Am 98:2073–2079. doi:2010.1785/0120070215

Berrocal J, Espinosa AF, Galdos J (1978) Seismological and geological aspects of Mantaro landslide in Peru. Nature 275:533–536

Brodsky EE, Gordeev E, Kanamori H (2003) Landslide basal friction as measured by seismic waves. Geophys Res Lett 30(24):2236. doi:2210.1029/2003GL018485

Dahlen FA (1993) Single-force representation of shallow landslide sources. Bull Seismol Soc Am 83:130–143

Deparis J, Jongmans D, Cotton F, Baillet L, Thouvenot F, Hantz D (2008) Analysis of rock-fall and rock-fall avalanche seismograms in the French Alps. Bull Seismol Soc Am 98:1781–1796. doi:1710.1785/0120070082

Eissler HK, Kanamori H (1987) A single force model for the 1975 Kalapana, Hawaii, earthquake. J Geophys Res 92:4827–4836

Huang NE, Wu Z (2008) A review on Hilbert-Huang transform: Method and its applications to geophysical studies. Rev Geophys 46:RG2006, doi: 2010.1029/2007RG000228

Huang NE, Long SR, Shen Z (1996) The mechanism for frequency downshift in nonlinear wave evolution. Adv Appl Mechanics 32:59–117

Hungr O, Evans SG, Bovis MJ, Hutchinson JN (2001) A review of the classification of landslides of the flow type. Environ Eng Geosci 7:221–238

Kanamori H, Given JW (1982) Analysis of long-period seismic waves excited by the May 18, (1980), eruption of Mount St. Helens-a terrestrial monopole. J Geophys Res 87:5422–5432

Kanamori H, Given JW, Lay T (1984) Analysis of seismic body waves excited by the Mount St. Helens eruption of May 18, 1980. J Geophys Res 89:1856–1866

Kao H, Shan S-J (2004) The Source-Scanning Algorithm: mapping the distribution of seismic sources in time and space. Geophys J Int 157:589–594

Kao H, Shan S-J (2007) Rapid identification of earthquake rupture plane using Source-Scanning Algorithm. Geophys J Int 168:1011–1020

Kao H, Jian P-R, Ma K-F, Huang B-S, Liu C-C (1998) Moment-tensor inversion for offshore earthquakes east of Taiwan and their implications to regional collision. Geophys Res Lett 25:3619–3622

Kao H, Shan S-J, Dragert H, Rogers G, Cassidy JF, Ramachandran K (2005) A wide depth distribution of seismic tremors along the northern Cascadia margin. Nature 436:841–844

La Rocca M, Galluzzo D, Saccorotti G, Tinti S, Cimini GB, Del Pezzo E (2004) Seismic signals associated with landslides and with a tsunami at Stromboli Volcano, Italy. Bull Seismol Soc Am 94:1850–1867

Norris RD (1994) Seismicity of rock-falls and avalanches at three cascade range volcanoes: implications for seismic detection of hazardous mass movements. Bull Seismol Soc Am 84:1925–1939

Rosenberger A (2010) Real-time ground motion analysis: distinguishing P- and S-arrivals in a noisy environment. Bull Seismol Soc Am 100(3):1252–1262. doi:1210.1785/0120090265

Tsai Y-B, Wu H-H (1997) A study of the errors in locating earthquakes due to the geometry of the Taiwan seismic network. Terr Atmos Oceanic Sci 8:355–370

H. Kao (✉) · A. Rosenberger
Geological Survey of Canada, Pacific Geoscience Centre,
9860 West Saanich Road, Sideny, BC V8L 4B2, Canada
e-mail: hkao@nrcan.gc.ca

C.-W. Kan · R.-Y. Chen · C.-H. Chang · T.-C. Shin · P.-L. Leu · K.-W. Kuo
Central Weather Bureau,
64, Gongyuan Road, Taipei 10048, Taiwan

W.-T. Liang
Institute of Earth Sciences, Academia Sinica,
128, Sec. 2, Academia Road, Nangang, Taipei 11529, Taiwan